# Numerical study on the influence of hydrogen addition on soot formation in a laminar ethylene–air diffusion flame

Hongsheng Guo [a,*], Fengshan Liu [a], Gregory J. Smallwood [a], Ömer L. Gülder [b]

[a] *Institute for Chemical Process and Environmental Technology, National Research Council of Canada, 1200 Montreal Road, Building M-9, Ottawa, Ontario, K1A 0R6 Canada*
[b] *Institute for Aerospace Studies, University of Toronto, 4925 Dufferin Street, Toronto, Ontario, M3H 5T6 Canada*

## Abstract

The influence of hydrogen addition to the fuel of an atmosphere pressure coflow laminar ethylene–air diffusion flame on soot formation was studied by numerical simulation. A detailed gas-phase reaction mechanism, which includes aromatic chemistry up to four rings, and complex thermal and transport properties were used. The fully coupled elliptic governing equations were solved. The interactions between soot and gas-phase chemistry were taken into account. Radiation heat transfer from $CO_2$, $CO$, $H_2O$, and soot was calculated using the discrete-ordinates method coupled to a statistical narrow-band-correlated $K$-based wide-band model. The predicted results were compared with the available experimental data and analyzed. It is indicated that the addition of hydrogen to the fuel in an ethylene–air diffusion flame suppresses soot formation through the effects of dilution and chemistry. This result is in agreement with available experiments. The simulations further suggest that the chemically inhibiting effect of hydrogen addition on soot formation is due to the decrease of hydrogen atom concentration in soot surface growth regions and higher concentration of molecular hydrogen in the lower flame region.

## 1. Introduction

The suppression of H atom concentration in flames accompanied by the suppression of flame luminosity due to carbon was observed by Arthur [1] more than 50 years ago. During the thermal decomposi-tion of natural gas, it was shown that dilution by hydrogen slows down the formation of carbon black particles [2]. In the experimental study of a coflow methane–air diffusion flame, Tesner et al. [3] noted that soot yield decreases with increase of the hydrogen fraction in methane. Dearden and Long [4] found that the addition of hydrogen to fuel results in reduction in sooting rates for ethylene or propane diffusion flames on a Wolfhard–Parker burner. Du et al. [5] observed that hydrogen addition to fuel results in a substantial decrease in soot particle inception limit

* Corresponding author. Fax: +1 (613) 957 7869.
*E-mail address:* hongsheng.guo@nrc-cnrc.gc.ca
(H. Guo).

for ethylene, propane, and butane counterflow diffusion flames. These investigations demonstrated that the addition of hydrogen to a hydrocarbon fuel in diffusion flames results in an overall suppression of soot formation. However, the relative contributions of dilution and direct chemical interaction to soot formation were not investigated.

In the experimental study of coflow laminar diffusion flames, Gülder et al. [6] first demonstrated that for an ethylene–air diffusion flame, the addition of hydrogen to fuel suppresses soot formation through both dilution and chemistry effects. However, the mechanism of the chemically inhibiting effect of hydrogen addition was not explained. Explaining the results of Gülder et al. [6], Glassman [7] proposed that the chemically inhibiting effect of hydrogen on soot formation might be that the rate of decomposition of vinyl to acetylene is slower than vinyl plus $H_2$ to reform ethylene plus an H atom.

In the present paper, we use numerical methods to further investigate the influence of hydrogen addition to fuel on soot formation in a coflow laminar ethylene–air diffusion flame. The objective is to use the details from the simulation to gain further insight into the phenomena that have been observed experimentally by Gülder et al. [6], particularly the chemically inhibiting effect of hydrogen addition on soot formation. Computationally, we employed the primitive variable method in which the fully elliptic governing equations were solved with detailed gas-phase chemistry and complex thermal and transport properties. For the soot process, a modified two-equation soot model was used.

## 2. Governing equations and numerical model

### 2.1. Flame configuration

The flame configuration studied is a coflow axisymmetric laminar diffusion flame [6]. The flames were generated at atmosphere pressure with a burner in which the fuel stream flows from a 10.9-mm-inner-diameter vertical tube, and the oxidant (air) flows from the annular region between the fuel tube and a 100-mm-diameter concentric tube. The wall thickness of the fuel tube is 0.95 mm.

### 2.2. Gas-phase governing equations

The numerical model includes fully elliptic governing equations for conservation of mass, momentum, energy, gas species mass fractions, soot mass fraction, and soot number density. In cylindrical coordinates $(r, z)$, the governing equations for the gas phase are [8] as follows.

Continuity,

$$\frac{\partial}{\partial r}(r\rho v) + \frac{\partial}{\partial z}(r\rho u) = 0; \tag{1}$$

Axial momentum,

$$\rho v \frac{\partial u}{\partial r} + \rho u \frac{\partial u}{\partial z}$$
$$= -\frac{\partial p}{\partial z} + \frac{1}{r}\frac{\partial}{\partial r}\left(r\mu\frac{\partial u}{\partial r}\right) + 2\frac{\partial}{\partial z}\left(\mu\frac{\partial u}{\partial z}\right)$$
$$- \frac{2}{3}\frac{\partial}{\partial z}\left(\frac{\mu}{r}\frac{\partial}{\partial r}(rv)\right) - \frac{2}{3}\frac{\partial}{\partial z}\left(\mu\frac{\partial u}{\partial z}\right)$$
$$+ \frac{1}{r}\frac{\partial}{\partial r}\left(r\mu\frac{\partial v}{\partial z}\right) + \rho g_z; \tag{2}$$

Radial momentum,

$$\rho v \frac{\partial v}{\partial r} + \rho u \frac{\partial v}{\partial z}$$
$$= -\frac{\partial p}{\partial r} + \frac{\partial}{\partial z}\left(\mu\frac{\partial v}{\partial z}\right) + \frac{2}{r}\frac{\partial}{\partial r}\left(r\mu\frac{\partial v}{\partial r}\right)$$
$$- \frac{2}{3}\frac{1}{r}\frac{\partial}{\partial r}\left(\mu\frac{\partial}{\partial r}(rv)\right) - \frac{2}{3}\frac{1}{r}\frac{\partial}{\partial r}\left(r\mu\frac{\partial u}{\partial z}\right)$$
$$+ \frac{\partial}{\partial z}\left(\mu\frac{\partial u}{\partial r}\right) - \frac{2\mu v}{r^2} + \frac{2}{3}\frac{\mu}{r^2}\frac{\partial}{\partial r}(rv)$$
$$+ \frac{2}{3}\frac{\mu}{r}\frac{\partial u}{\partial z}; \tag{3}$$

Energy,

$$c_{\mathrm{p}}\left(\rho v \frac{\partial T}{\partial r} + \rho u \frac{\partial T}{\partial z}\right)$$
$$= \frac{1}{r}\frac{\partial}{\partial r}\left(r\lambda\frac{\partial T}{\partial r}\right) + \frac{\partial}{\partial z}\left(\lambda\frac{\partial T}{\partial z}\right)$$
$$- \sum_{k=1}^{\mathrm{KK}+1}\left[\rho c_{\mathrm{p}k}Y_k\left(V_{kr}\frac{\partial T}{\partial r} + V_{kz}\frac{\partial T}{\partial z}\right)\right]$$
$$- \sum_{k=1}^{\mathrm{KK}+1} h_k W_k \omega_k + q_r; \tag{4}$$

Gas species,

$$\rho v \frac{\partial Y_k}{\partial r} + \rho u \frac{\partial Y_k}{\partial z} = -\frac{1}{r}\frac{\partial}{\partial r}(r\rho Y_k V_{kr})$$
$$- \frac{\partial}{\partial z}(\rho Y_k V_{kz}) + W_k \omega_k,$$
$$k = 1, 2, \ldots, \mathrm{KK}; \tag{5}$$

where $u$ and $v$ are the velocities in axial $(z)$ and radial $(r)$ directions, respectively; $T$ the temperature of the mixture; $\rho$ the density of the mixture (soot and gas); $W_k$ the molecular weight of the $k$th gas species; $\lambda$ the mixture thermal conductivity; $c_{\mathrm{p}}$ the specific heat of the mixture under constant pressure; $c_{\mathrm{p}k}$ the specific heat of the $k$th gas species under constant pressure; and $\omega_k$ the mole production rate of the $k$th gas species

per unit volume. The production rates of gas species include the contribution due to soot inception, surface growth, and oxidation. Quantity $h_k$ denotes the specific enthalpy of the $k$th gas species; $g_z$ the gravitational acceleration in $z$ direction; $\mu$ the viscosity of the mixture; $Y_k$ the mass fraction of the $k$th gas species; $V_{kr}$ and $V_{kz}$ the diffusion velocities of the $k$th gas species in $r$ and $z$ directions; and KK the total gas-phase species number. The quantities with subscript KK + 1 correspond to those of soot. As an approximation, the thermal properties of graphite, obtained from JANAF thermochemical tables [9], were used to represent those of soot.

The last term on the right-hand side of Eq. (4) is the source term due to radiation heat transfer. It was obtained by the discrete ordinate method coupled to a statistical narrow-band-correlated K (SNBCK)-based wide-band model for properties of CO, $CO_2$, $H_2O$, and soot [10]. The spectral absorption coefficient of soot was obtained by Rayleigh's theory for small particles and the refractive index of soot due to Dalzell and Sarofim [11] as $5.5 f_v/\lambda$, with $f_v$ being the soot volume fraction and $\lambda$ the wavelength.

The diffusion velocity is written as

$$V_{kx_i} = V_{ox_i} + V_{Tkx_i} + V_{cx_i}, \quad k = 1, 2, \dots, KK,$$
$$x_i = r, z, \tag{6}$$

where $V_{ox_i}$, $V_{Tkx_i}$, and $V_{cx_i}$ are respectively the ordinary, the thermal diffusion, and the correction diffusion velocity in $x_i$ ($r$ or $z$) direction for the $k$th gas species. The mixture-average formulation [12] was used to calculate the ordinary diffusion velocity. A previous study [13] showed that only the thermal diffusion of lighter species is significant in affecting soot formation. Therefore, only the thermal diffusion velocities of $H_2$, H, and He were considered by the method given in Ref. [12], while those of all other species were set as zero in this paper. The correction diffusion velocity $V_{cx_i}$ was used to ensure that the net diffusive flux of all gas species and soot is zero.

### 2.3. Soot model

A simplified two-equation model developed by Leung et al. [14] and Fairwhether et al. [15] has been successfully used in our previous studies [13,16] for the simulations of ethylene/air diffusion flames. It was proved that the model can capture the primary features of soot formation in ethylene/air diffusion flames. This model is therefore also used in this paper with modifications made to both the soot nucleation and the surface growth processes.

Two transport equations were solved for soot mass fraction and number density, respectively. They are

$$\rho v \frac{\partial Y_s}{\partial r} + \rho u \frac{\partial Y_s}{\partial z} = -\frac{1}{r}\frac{\partial}{\partial r}(r\rho V_{T,r} Y_s)$$
$$- \frac{\partial}{\partial z}(\rho V_{T,z} Y_s) + S_m, \tag{7}$$

$$\rho v \frac{\partial N}{\partial r} + \rho u \frac{\partial N}{\partial z} = -\frac{1}{r}\frac{\partial}{\partial r}(r\rho V_{T,r} N)$$
$$- \frac{\partial}{\partial z}(\rho V_{T,z} N) + S_N, \tag{8}$$

where $Y_s$ is soot mass fraction, and $N$ is soot number density defined as the particle number per unit mass of mixture. Quantities $V_{T,r}$ and $V_{T,z}$ are the particle thermophoretic velocities in $r$ and $z$ directions, respectively. They were obtained by the expression [17]

$$V_{T,x_i} = -0.55 \frac{\mu}{\rho T}\frac{\partial T}{\partial x_i}, \quad x_i = r, z. \tag{9}$$

The source term $S_m$ in Eq. (7) consists of the contributions of soot nucleation ($\omega_n$), surface growth ($\omega_g$) and oxidation ($\omega_o$), i.e.,

$$S_m = \omega_n + \omega_g - \omega_o. \tag{10}$$

Being different from the previous studies [13,16] where acetylene was assumed to be the sole chemical species responsible for soot particle nucleation and surface growth, the soot nucleation and surface growth submodels were modified in this paper. These modifications are necessary in order to account for the chemical effect of hydrogen addition on soot formation, as the acetylene-based model used in the previous studies [13,16] is unable to elucidate the chemical role of hydrogen.

Although soot nucleation is a complex process that has not been fully understood, it is widely accepted [18,19] that the polycyclic aromatic hydrocarbons (PAH) develop into soot particle nuclei when their structures reach a large enough size. Following Frenklach and Wang [19], the nucleation of soot was assumed to be due to PAH coagulation, i.e., a coalescence of two PAH species into a dimer:

$$PAH + PAH \Rightarrow dimmer. \tag{R1}$$

The PAH assumed for the nucleation of soot particle is pyrene ($A_4$). The soot mass growth rate due to nucleation was calculated as [19]

$$\omega_n = 2 N_{CPAH} C_{mass} R_{in}, \tag{11}$$

where $N_{CPAH}$ is the number of carbon atoms in nucleation PAH, $C_{mass}$ is the mass of a carbon atom, and $R_{in}$ is the soot particle nucleation rate (particles/cm$^3$ s), given as

$$R_{in} = 2.2 \left[\frac{4\pi \kappa_B T}{C_{mass} N_{CPAH}}\right]^{1/2} d_{PAH}^2 N_A^2 [PAH]^2, \tag{12}$$

where $\kappa_B$ is the Boltzmann constant ($1.3807 \times 10^{-16}$ erg/K), $N_A$ is the Avogadro constant ($6.022 \times 10^{23}$ molecules/mol), and [PAH] is the mole concentration of the nucleation PAH species (mol/cm$^3$). The quantity $d_{PAH}$ is the collision diameter of the nucleation PAH. It was assumed that $d_{PAH}$ is related to its carbon atom content as [19]

$$d_{PAH} = 1.395\sqrt{2N_{CPAH}} \text{ Å}. \tag{13}$$

The surface growth and oxidation were assumed to follow the H-abstraction and acetylene addition (HACA) reaction sequence given by Appel et al. [20]. The rates of surface growth and soot oxidation ($\omega_g$ and $\omega_o$) were calculated based on the kinetics data of Table 3 in [20]. However, modifications were made for the parameter $\alpha$, the fraction of the reactive surface available for chemical reactions, and the reaction probability of soot oxidation due to the attack of OH ($\phi_{OH}$). A similar correlation to that of Xu et al. [21] for the parameter $\alpha$ was used in this paper, i.e.,

$$\alpha = 0.0045 \exp(9000/T). \tag{14}$$

Further discussion on parameter $\alpha$ will be given later. A constant 0.06 was used for the reaction probability of soot oxidation due to the attack of OH. This value is lower than that recommended by Neoh et al. [22], but best fits the experimental data [6] in terms of flame height. The modification to this value does not significantly affect the predicted peak soot volume fraction, since the peak soot volume fraction occurs in a region where soot growth rate is much faster than that of oxidation.

The source term $S_N$ in Eq. (8) accounts for soot particle nucleation and agglomeration, and was calculated as

$$S_N = R_{in} - 2C_a \left(\frac{6M_{C(s)}}{\pi \rho_{C(s)}}\right)^{1/6} \left(\frac{6\kappa T}{\rho_{C(s)}}\right)^{1/2} \\ \times [C(s)]^{1/6} [\rho N]^{11/6}, \tag{15}$$

where $R_{in}$ is the particle nucleation rate given by Eq. (12), $\rho_{C(s)}$ is the soot density (1.9 g/cm$^3$), $[C(s)]$ is the mole concentration of soot particle (mol/cm$^3$), $M_{C(s)}$ is the molar mass of soot (12.0 g/mol), and $C_a$ is the agglomeration rate constant for which a value of 1.0 was used.

### 2.4. Numerical model

Low Mach number assumption was adopted. The governing equations were discretized using the finite volume method in axisymmetric cylindrical coordinates. The SIMPLE numerical scheme [23] was used to handle the pressure and velocity coupling. The diffusion terms in the conservation equations were dis-

cretized by the central difference method and the convective terms were discretized by the upwind difference method. The governing equations of gas species, soot mass fraction, and soot number density were solved in a fully coupled fashion at each control volume [24] in order to speed up the convergent process, while those of momentum, energy, and pressure correction were solved using the tri-diagonal matrix algorithm (TDMA).

The computational domain covers an area from 0 to 3.0 cm in the radial direction and 0 to 11.0 cm in the axial direction. It has been checked by a sensitivity calculation that this computational domain is sufficiently large and thus the boundary location does not influence the simulation results. The inflow boundary ($z = 0$ cm) corresponds to the region immediately above the fuel nozzle. Totally $160(z) \times 81(r)$ nonuniform grids were used in the simulations, with finer grids placed in the primary reaction zone and near the fuel nozzle exit region. It has been checked that the further increase of grid number does not significantly influence the simulation results.

The chemical reaction mechanism used is that developed in [20]. The thermal and transport properties were obtained by using the algorithms given in Refs. [12,25].

## 3. Results and discussion

The above numerical model was used to simulate coflow laminar ethylene–air and (ethylene + hydrogen)–air diffusion flames. In addition, we also calculated (ethylene + helium)–air diffusion flames to identify the chemically inhibiting effect of hydrogen addition on soot formation. The reason to choose helium as an additive is that it has a dilution effect similar to that of hydrogen and is chemically inert.

The flames were generated by the burner described in Section 2.1. The volume flow rates of air and ethylene are, respectively, 284 L/min and 194 ml/min for all the flames, while hydrogen or helium is added to the fuel. The amounts of the added hydrogen and helium varied, so that the volume fractions of hydrogen and helium in the fuel stream changed from 0 to 24% and 0 to 30%, respectively, with interval being 5%. The maximum values of the added hydrogen and helium were selected to match the experimental conditions in [6].

Fig. 1 shows the soot volume fractions obtained by the experiment [6] and the present simulation for the pure ethylene–air diffusion flame. It is observed that the computation captured the general features of soot, although it failed to predict soot in the centerline region. The value of the peak soot volume fraction and the distribution of soot volume fraction obtained by
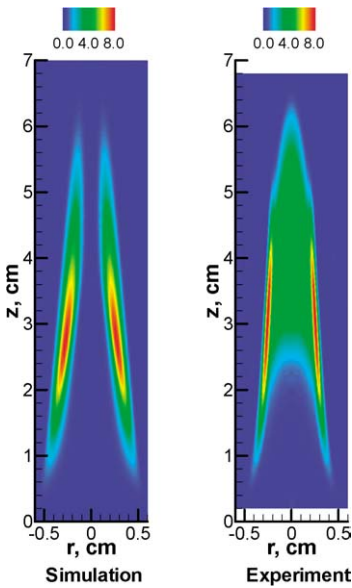
Fig. 1. Predicted and measured [6] soot volume fractions (ppm) of pure ethylene flame.

the simulation are similar to those from the experiment. The failure to predict the soot in the centerline region may be attributed to the simplification of the soot model.

Now we examine the effects of hydrogen and helium addition on soot formation. Fig. 2 displays the integrated soot volume fractions, obtained by integrating soot volume fraction with respect to radius, versus the distance ($z$) above the burner exit for the pure ethylene–air flame, the (24% $H_2$ + 76% $C_2H_4$)–air flame, and the (30% He + 70% $C_2H_4$)–air flame. It illustrates that the addition of either hydrogen or

helium to the fuel suppresses the formation of soot in an ethylene–air diffusion flame. However, although the fraction of added hydrogen (24%) is lower than that of added helium (30%) in Fig. 2, the reduction of soot volume fraction due to the addition of hydrogen is more significant. This is in agreement with the experimental observation by Gülder et al. [6]. It implies that the addition of hydrogen is more efficient than that of helium to suppress soot formation in an ethylene–air diffusion flame.

The variation of the normalized maximum soot volume fraction, defined as the ratio of the maximum soot volume fraction in the diluted flames to that in the pure ethylene–air flame, versus the fraction of hydrogen or helium is depicted in Fig. 3. The experimental results [6] are also shown for comparison. It is noted that the simulations successfully reproduced the experimental phenomenon. This means that the soot model captured the primary feature of soot formation in an ethylene–air diffusion flame, especially the chemical effect of hydrogen addition on soot.

When hydrogen or helium is added to the fuel, soot formation can be affected owing to the thermal, the dilution, and the direct chemical reaction effect. Since both hydrogen and helium are transparent in terms of radiation heat transfer and their specific heats are smaller than that of ethylene, there is little thermal effect that causes the reduction in soot formation when they are added to fuel. For example, the specific heats at constant pressure for hydrogen, helium, and ethylene at 1700 K are, respectively, 33, 21, and 114 J/(mol K).

Unlike hydrogen, helium is an inert species. Therefore, the reduction of soot formation because of its addition to ethylene is the result of dilution effect.
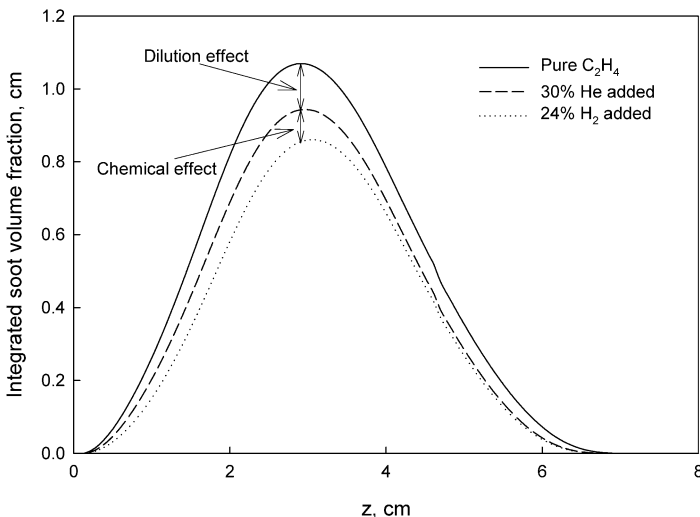


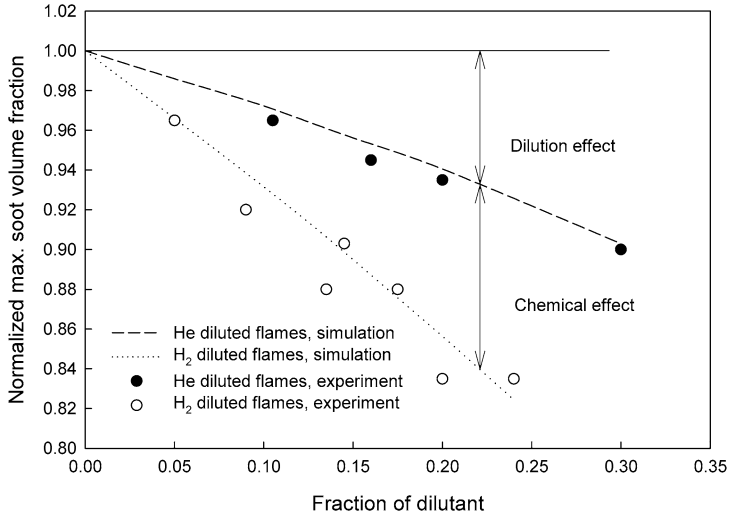Fig. 2. Integrated soot volume fractions for three flames.

Fig. 3. Normalized maximum soot volume fraction versus the fraction of diluent.
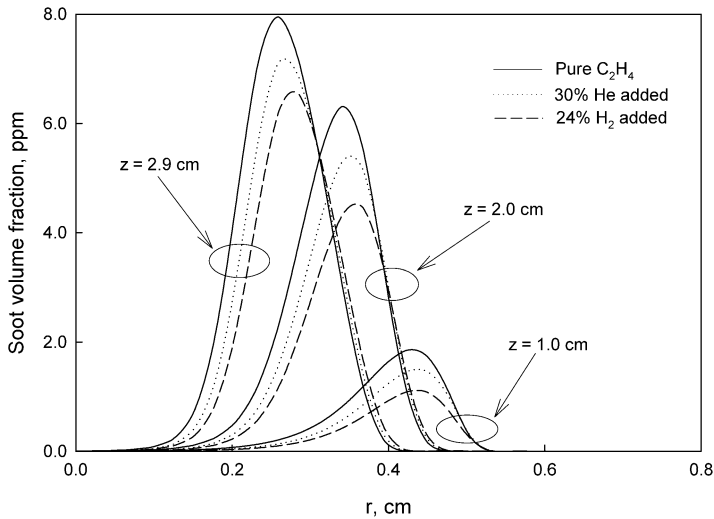


Fig. 4. Radial distributions of soot volume fraction at three axial heights.

Hydrogen has specific heat and transport properties similar to those of helium, and, as a fuel, it has an adiabatic flame temperature similar to that of ethylene. Its dilution effect on soot formation is expected to be similar to that of helium. However, being different from helium, the added hydrogen actively participates in chemical reactions. The difference in the soot yield between the helium- and the hydrogen-diluted flames should be the result of the chemically inhibiting effect of hydrogen. This chemically inhibiting effect causes hydrogen to be more efficient than helium at suppressing soot yields in ethylene diffusion flames. We will analyze the chemically inhibiting effect of hydrogen addition on soot formation by comparing the results of hydrogen- and helium-diluted flames.

In the following discussion, we will take the 24% hydrogen-diluted and the 30% helium-diluted flames as examples, as shown in Fig. 2.

Figs. 4–6 compare the radial profiles of the soot volume fraction, the rates of soot nucleation and surface growth at three axial heights for the pure ethylene, the 30% helium-diluted, and the 24% hydrogen-diluted flames. The surface growth rate in Fig. 6 was not corrected by oxidation rate, which will be discussed separately later. First, it is observed that the soot volume fraction of the hydrogen-diluted flame is lower than that of the helium-diluted flame in most regions (Fig. 4). This agrees with the experimental observation [6] and the result in Fig. 2. Secondly, the surface growth rate is much bigger than
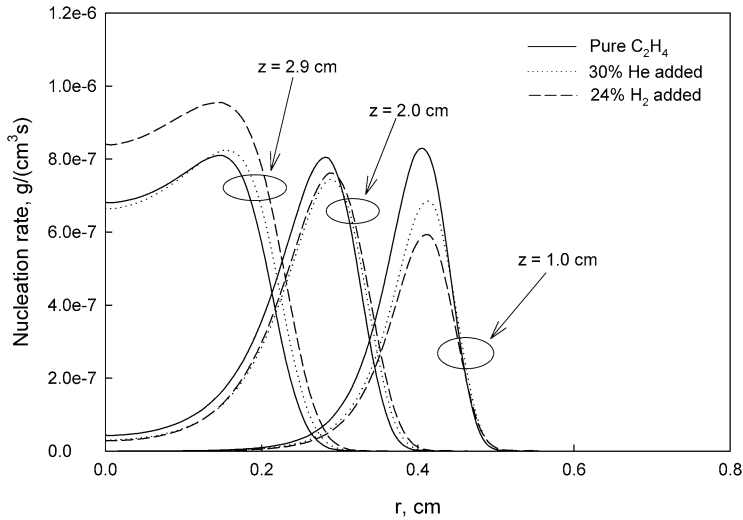
Fig. 5. Radial distributions of soot nucleation rate at three axial heights.
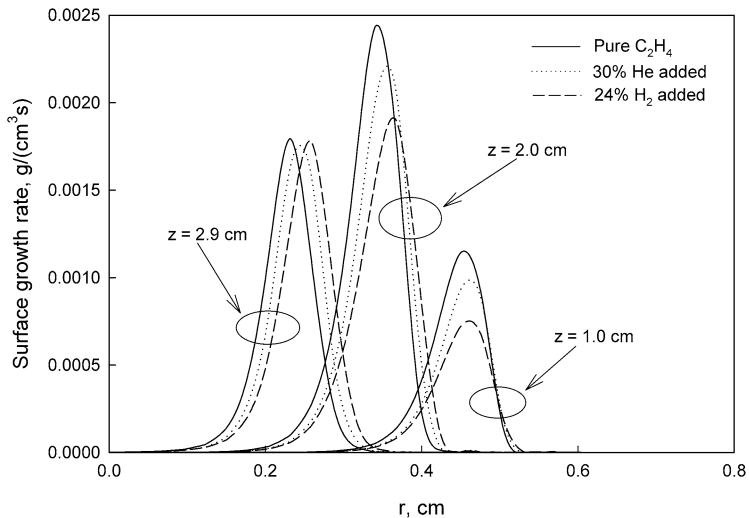


Fig. 6. Radial distributions of surface growth rate at three axial heights.

the nucleation rate for each flame. This is consistent with the current understanding of soot formation; i.e., surface growth contributes most soot mass in a flame.

At the lower flame region ($z = 1.0$ cm), both the nucleation and the surface growth rates in the hydrogen-diluted flame are lower than those in the helium-diluted flame. However, with the increase of $z$, the nucleation rate of the hydrogen-diluted flame gradually becomes higher than that of the helium-diluted flame. This is different than the observed variation in soot volume fraction change between the hydrogen and the helium-diluted flames in Fig. 4. However, it should be noted that the contribution of

nucleation to total soot is not significant in a diffusion flame.

On the other hand, the difference in surface growth rate (Fig. 6) between the helium and the hydrogen-diluted flames is in general consistent with that in soot volume fraction in Fig. 4 until $z = 2.0$ cm; i.e., the surface growth rate in the hydrogen-diluted flame is lower than that in the helium-diluted flame. However, this difference contradicts that of the soot volume fraction at $z = 2.9$ cm, where the disparity of the peak surface growth rates between the hydrogen and the helium-diluted flames becomes negligible, while the soot volume fraction of the helium-diluted flame is still higher. This is because significant soot is formed
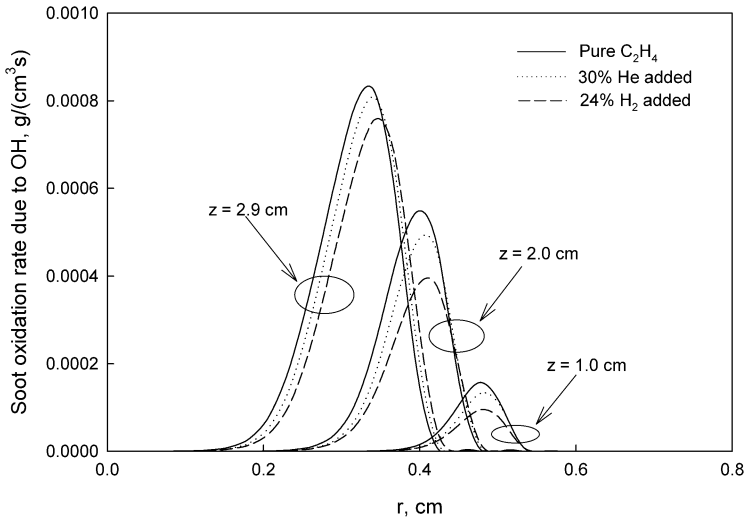
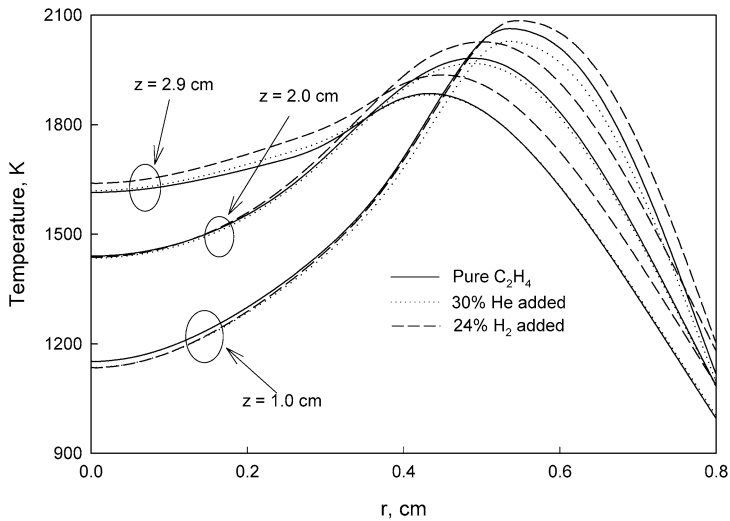Fig. 7. Radial distributions of soot oxidation rate due to OH at three axial heights.



Fig. 8. Radial distributions of temperature at three axial heights.

at $z < 2.9$ cm and is then transported to the upper region.

When $z$ becomes greater than about 2.9 cm, it can be observed from Figs. 1 and 2 that soot volume fraction begins to decrease with increasing $z$, since the oxidation of soot becomes significant and eventually will dominate the soot formation rate. Fig. 7 displays the radial profiles of soot oxidation rate due to the attack of OH, the most important oxidant for soot, at three axial heights. The oxidation rate increases monotonously with the rise of $z$ until $z = 2.9$ cm.

Based on the soot nucleation model (reaction (R1) and Eq. (12)), two factors may directly affect the nucleation rate in a flame, i.e., temperature and nucleation PAH concentration. The nucleation rate is pro-

portional to the square root of temperature and the square of the nucleation PAH concentration. It is expected that the nucleation PAH concentration has a stronger influence on the nucleation rate than temperature. Fig. 8 displays the radial temperature profiles at three axial heights. The temperature of the hydrogen-diluted flame is always slightly higher than that of the helium-diluted flame. This is mainly because hydrogen is a fuel and releases heat during chemical reactions, while helium is an inert species. As a result, temperature is not a factor causing the lower nucleation rate in the hydrogen-diluted flame than in the helium-diluted flame at $z = 1.0$ cm.

The concentration profiles of nucleation PAH, pyrene, at three axial heights are shown in Fig. 9.
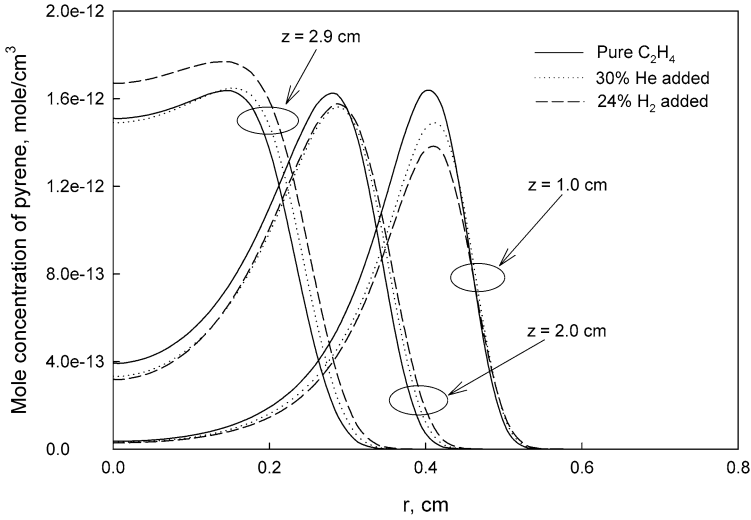
Fig. 9. Radial distributions of pyrene concentration at three axial heights.
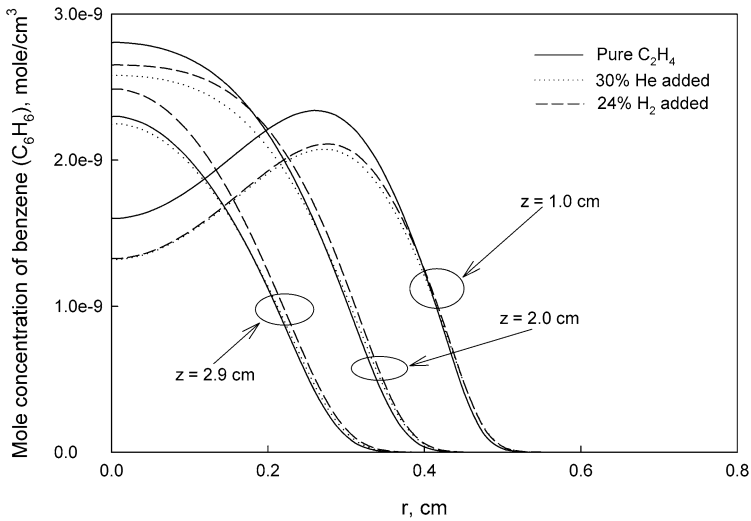


Fig. 10. Radial distributions of benzene concentration at three axial heights.

At $z = 1.0$ cm, the concentration of pyrene in the hydrogen-diluted flame is lower than that in the helium-diluted flame. However, with the increase of $z$, the difference in the concentrations of pyrene between the hydrogen and the helium-diluted flames gradually decreases, and finally the concentration of pyrene in the hydrogen-diluted flame becomes higher. This variation trend is similar to that observed in the nucleation rates shown in Fig. 5. Therefore, it can be concluded that the variation of the difference in the nucleation rate between the hydrogen and the helium-diluted flames is caused by the difference in the concentration of nucleation species. When $z = 1.0$ cm, the lower concentration of pyrene causes the lower nucleation rate in the hydrogen-diluted flame. With

the increase of $z$, the concentration of pyrene in the hydrogen-diluted flame gradually becomes higher than that in the helium-diluted flame (Fig. 9) which leads to the higher nucleation rate at the upper region of the hydrogen-diluted flame. To explain the variation trend of pyrene, we will examine the profiles of some other species.

Figs. 10–13 show the radial profiles of benzene ($C_6H_6$), acetylene ($C_2H_2$), and atomic and molecular hydrogen at the three axial heights.

Benzene is the first aromatic ring. Once it is formed, the aromatic rings grow essentially through a sequential process: HACA. The key reactions in the HACA reaction sequence can be represented by
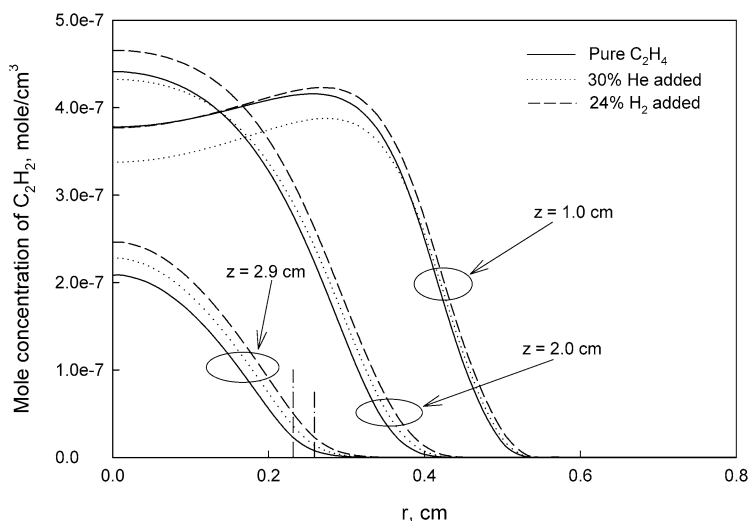
$$A_i + H \Leftrightarrow A_i \bullet + H_2, \tag{R2}$$

Fig. 11. Radial distributions of acetylene ($C_2H_2$) concentration at three axial heights. The vertical dash–dot lines indicate the radial positions of the peak surface growth rates in the hydrogen- and helium-diluted flames at $z = 2.9$ cm (the left one is for the helium-diluted flame and the right one is for the hydrogen-diluted flame).
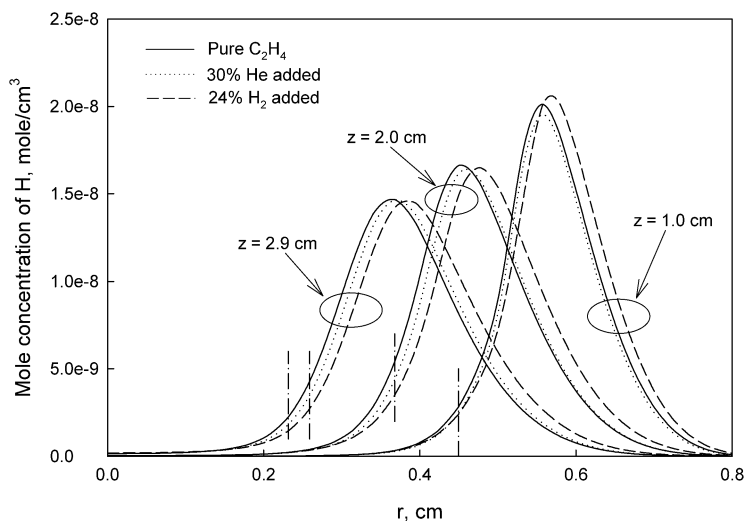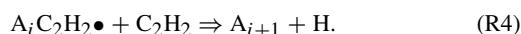


Fig. 12. Radial distributions of atomic hydrogen (H) concentration at three axial heights. The vertical dash–dot lines indicate radial positions of the peak surface growth rates (at $z = 2.9$ cm, the left one is for the helium-diluted flame and the right one is for the hydrogen-diluted flame).

$$A_i\bullet + C_2H_2 \Leftrightarrow A_iC_2H_2\bullet, \qquad (R3)$$

$$A_iC_2H_2\bullet + C_2H_2 \Rightarrow A_{i+1} + H. \qquad (R4)$$

Therefore, the factors that directly affect the formation of a large PAH include the concentration of the first aromatic ring—benzene ($A_1$), the temperature, and the concentrations of species $C_2H_2$, $H_2$, and H.

Pyrene is a four-ring PAH ($A_4$). Comparing the concentration profiles of pyrene and benzene in Figs. 9 and 10, it is found that while the concentration of benzene is higher in most regions, the concentration of pyrene is smaller at $z = 1.0$ cm but higher

at $z = 2.0$ and 2.9 cm in the hydrogen-diluted flame than in the helium-diluted flame. The concentration of acetylene (Fig. 11) in the hydrogen-diluted flame is always higher than those in the helium-diluted flame. The combined effects of the higher temperature and higher concentrations of benzene and acetylene in the hydrogen-diluted flame enhance the PAH growth rate and result in the higher concentration of pyrene at the upper region of the hydrogen-diluted flame. However, these factors cannot cause the lower concentration of pyrene at $z = 1.0$ cm in the hydrogen-diluted flame than in the helium-diluted flame. The difference in
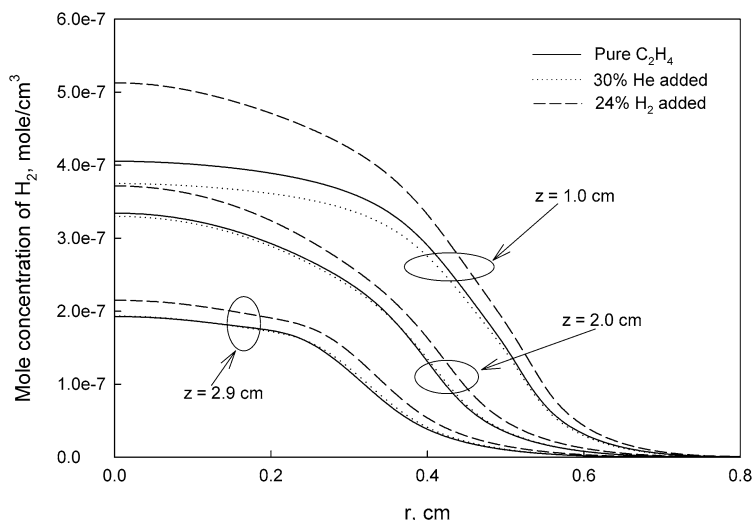
Fig. 13. Radial distributions of hydrogen ($H_2$) concentration at three axial heights.

the concentrations of atomic hydrogen (Fig. 12) between the hydrogen and the helium-diluted flames is negligible in the peak pyrene concentration regions. Consequently atomic hydrogen is not a factor causing the lower pyrene concentration at $z = 1.0$ cm in the hydrogen-diluted flame either. The lower concentration of pyrene at $z = 1.0$ cm in the hydrogen-diluted flame is actually because of the higher concentration of molecular hydrogen, as shown in Fig. 13, which causes the bigger reverse rate of the hydrogen abstraction reaction (R2), and thus reduces the PAH growth rate at $z = 1.0$ cm of the hydrogen-diluted flame. This leads to the lower concentration of pyrene and the lower nucleation rate at $z = 1.0$ cm in the hydrogen-diluted flame, despite the more benzene there. With the increase of $z$, the molecular hydrogen from the parent fuel stream is quickly reduced and the difference in the concentrations of molecular hydrogen between the hydrogen- and the helium-diluted flames becomes smaller, causing less disparity in the reverse rates of reaction (R2).

The formation of benzene is closely related to acetylene ($C_2H_2$). The higher concentration of benzene in the hydrogen-diluted flame than in the helium-diluted flame results from more acetylene, as shown by Fig. 11, since less acetylene is consumed in the hydrogen-diluted flame. A sensitivity analysis reveals that the most significant destruction reaction of acetylene is $O + C_2H_2 = H + HCCO$. In the hydrogen-diluted flame, more molecular and atomic oxygen are consumed by hydrogen, leading to a lower rate of the acetylene destruction reaction and hence a higher concentration of acetylene.

Now we discuss the surface growth rates in the hydrogen- and helium-diluted flames. Based on the adopted HACA surface growth model [20], the soot surface growth rate equals $k_{C_2H_2}[C_2H_2]\alpha\chi_{CS}A_S/N_A$, where $k_{C_2H_2}$ is the per-site rate coefficient for acetylene addition, $[C_2H_2]$ is the mole concentration of acetylene, $\alpha$ is the fraction of available reactive surface, $A_S$ is the particle surface area, $N_A$ is Avogadro's number, and $\chi_{CS}$ is the number density of surface sites for acetylene addition. It is seen that the factors directly affecting surface growth rate include the per-site acetylene addition rate ($k_{C_2H_2}[C_2H_2]$), the particle surface area ($A_S$), the number density of surface sites ($\chi_S$), and $\alpha$.

At $z = 1.0$ and 2.0 cm, the surface growth rates of the hydrogen- and helium-diluted flames peak at almost the same radial positions, as shown in Fig. 6. The per-site acetylene addition rate depends on temperature and acetylene concentration. As discussed before, the temperature (Fig. 8) and acetylene concentration (Fig. 11) in the hydrogen-diluted flame are higher than in the helium-diluted flame. Accordingly, the addition of hydrogen tends to increase the per-site acetylene addition rate, compared to the addition of helium. Therefore, the per-site acetylene addition rate change is not a factor leading to the lower surface growth rate at $z = 1.0$ and 2.0 cm in the hydrogen-diluted flame.

Fig. 14 shows the particle surface area per unit volume ($A_S$, cm$^{-1}$). It is noted that the particle surface area in the hydrogen-diluted flame is lower than in the helium-diluted flame at all three axial heights. As a result, the particle surface area is a factor causing the lower surface growth rate at $z = 1.0$ and 2.0 cm in the hydrogen-diluted flame.

Particle surface area is proportional to the product of the particle number density and the square of the particle diameter. Fig. 15 illustrates the profiles of soot particle number density. It demonstrates
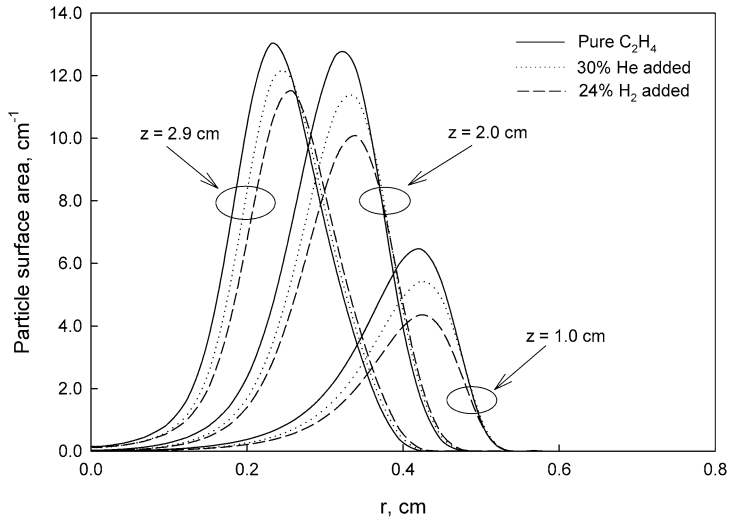
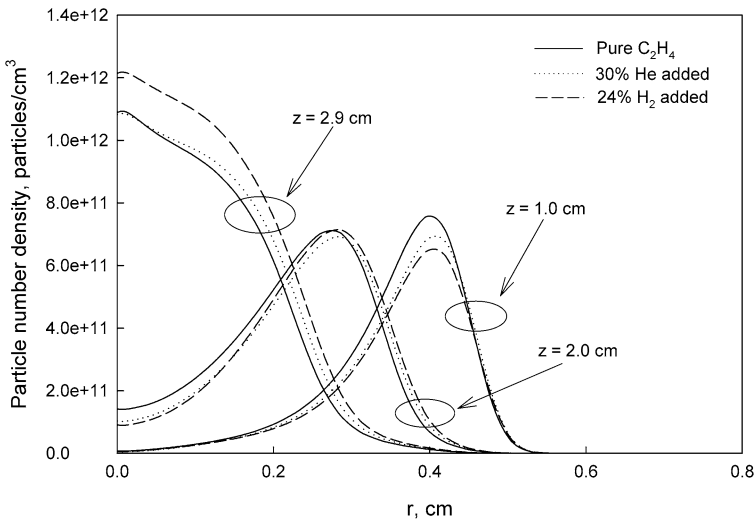Fig. 14. Particle surface area at three axial heights.



Fig. 15. Radial distributions of particle number density at three axial heights.

that at $z = 1.0$ cm, the particle number density in the hydrogen-diluted flame is lower than that in the helium-diluted flame, which is a direct consequence of the lower nucleation rate in the hydrogen-diluted flame (Fig. 5). The lower particle number density results in a smaller particle surface area at $z = 1.0$ cm in the hydrogen-diluted flame. However, at $z = 2.0$ cm, the particle number density of the hydrogen-diluted flame becomes higher than that of the helium-diluted flame. Therefore, the smaller particle surface area at $z = 2.0$ cm in the hydrogen-diluted flame than in the helium-diluted flame is because of the smaller particle size. Since pyrene was used as nucleation PAH in all the flames, the soot particle nuclei have the same size in the hydrogen and helium-diluted flames. This sug-

gests that the smaller particle size at $z = 2.0$ cm in the hydrogen-diluted flame is caused by the slower particle size growth rate after particles are incepted. The particle size growth rate is related to the specific soot surface growth rate, i.e., the surface growth rate per unit surface area. This quantity hence also depends on the per-site acetylene addition rate ($k_{C_2H_2}[C_2H_2]$), the number density of surface sites ($\chi_S$), and $\alpha$. As discussed before, the per-site acetylene addition rate is not a factor causing the lower growth rate in the hydrogen-diluted flame.

The distribution of the surface-site number density for acetylene addition ($\chi_{CS}$) is shown in Fig. 16. It is noted that the number density of surface sites for acetylene addition in the hydrogen-diluted flame
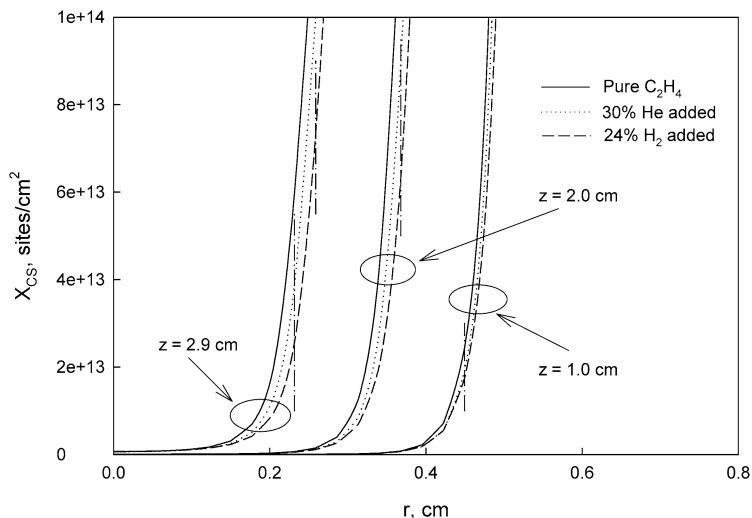
Fig. 16. Radial distributions of surface-site ($\chi_{CS}$) density at three axial heights. The vertical dash–dot lines indicate the radial positions of the peak surface growth rates in the hydrogen and helium-diluted flames (at $z = 2.9$ cm, the left one is for the helium-diluted flame and the right one is for the hydrogen-diluted flame).

is significantly lower than that in the helium-diluted flame at $z = 2.0$ cm. The lower number density of surface sites in the hydrogen-diluted flame results in both the lower specific surface growth rate and thus the smaller particle surface area than in the helium-diluted flame. Therefore, it is the lower surface-site number density of acetylene addition in the hydrogen-diluted flame that causes the lower surface growth rate in the hydrogen-diluted flame than in the helium-diluted flame at $z = 2.0$ cm.

The two key reactions in the HACA surface reaction sequence are

$$C_{soot}–H + H \Leftrightarrow C_{soot}· + H_2, \qquad (R5)$$

$$C_{soot}· + C_2H_2 \Rightarrow C_{soot}–H + H. \qquad (R6)$$
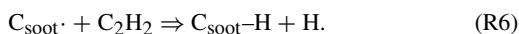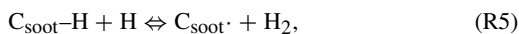
The former is the H-abstraction reaction to form the active site for acetylene addition, and the latter is the acetylene addition reaction. The H-abstraction reaction is reversible, but the calculation indicates that the rate of the reverse reaction is much smaller than that of the forward reaction. Fig. 12 illustrates that the concentration of atomic hydrogen at the surface growth regions (indicated by the vertical dash–dot lines) in the hydrogen-diluted flame is lower than that in the helium-diluted flame at $z = 2.0$ cm, although the peak values of the atomic hydrogen concentration in the two diluted flames are similar. This is because of the preferential diffusion of hydrogen. The lower concentration of atomic hydrogen in the surface growth region causes the lower forward rate of reaction (R5) and thus the smaller surface-site number density for acetylene addition in the hydrogen-diluted flame at $z = 2.0$ cm. Therefore, at $z = 2.0$ cm, the

lower concentration of atomic hydrogen in the surface growth region is the primary factor causing the smaller surface growth rate in the hydrogen-diluted flame.

It is also shown that at $z = 1.0$ cm, the concentrations of atomic hydrogen in the surface growth region are similar in the hydrogen- and helium-diluted flames, which leads to the similar surface-site number density in the two flames. As a consequence, the lower particle surface area and thus the lower surface growth rate at $z = 1.0$ cm in the hydrogen-diluted flame are because of the smaller nucleation rate that results from the higher concentration of molecular hydrogen.

As Figs. 5 and 6 show that surface growth contributes most soot and the growth rate reaches the maximum at $z = 2.0$ cm in a flame, the lower concentration of atomic hydrogen in the surface growth region is a primary factor causing the lower soot yield in the hydrogen-diluted flame than in the helium-diluted flame.

At $z = 2.9$ cm, it is observed that the peak surface growth rate positions are significantly different in the hydrogen- and the helium-diluted flames. This is perhaps because the temperature is lower at this axial height and the effect of acetylene on surface growth increases. Figs. 11 and 12 show that the concentration of acetylene in the peak growth region of the hydrogen-diluted flame is lower, but the situation reverses for the concentration of hydrogen atom. Overall they cause similar peak surface growth rates in the hydrogen- and helium-diluted flames at $z = 2.9$ cm, with that in the hydrogen-diluted flame being slightly higher. However, it should be noted that the surface

growth at $z = 2.9$ cm does not affect the global feature of soot distributions in the two flames, since most soot is formed at the lower flame region and the oxidation of soot becomes significant at $z = 2.9$ cm, as shown in Fig. 7.

Another factor affecting the surface growth rate is the fraction of available reactive surface, $\alpha$. It has been shown that this parameter depends on temperature [21,26]. However, there is a lack of a consistent correlation for the calculation of this parameter in the literature. The expression given in Eq. (14) was found to best fit the experimental results of [6]. The dependence of $\alpha$ on temperature in Eq. (14) is between those given in Refs. [21,26]. The increase of temperature causes a lower $\alpha$. Because of the higher temperature, $\alpha$ causes the lower surface growth rate in the hydrogen-diluted flame than in the helium-diluted flame. However, our test using a constant $\alpha$ also showed a lower soot volume fraction in the hydrogen-diluted flame than in the helium-diluted flame, although the difference between the two diluted flames was reduced.

Therefore, we can conclude that the addition of hydrogen to ethylene is more effective than that of helium at suppressing soot formation. It is because the addition of helium suppresses soot formation only through the dilution effect, while the addition of hydrogen suppresses soot formation through both dilution and chemical effects. The chemically inhibiting effect of hydrogen addition on soot formation is because of the reduced concentration of H in the surface growth region and the higher concentration of molecular hydrogen in the lower flame region. These two factors cause the lower H-abstraction rate in the PAH and particle surface growth processes of the hydrogen-diluted flame. This conclusion is different from Glassman's viewpoint that the chemically inhibiting effect of hydrogen on soot formation might be that the rate of decomposition of vinyl to acetylene is slower than vinyl plus $H_2$ to reform ethylene plus an H atom [7]. The agreement of the predicted soot formation with the available experimental data by Gülder et al. [6] supports the theory that the HACA reaction sequence plays an important role in PAH growth and soot surface growth processes in ethylene diffusion flames.

## 4. Conclusions

The influences of hydrogen addition to fuel on soot formation in an ethylene–air diffusion flame have been numerically studied by the simulations of axisymmetric, laminar, coflow ethylene–air, (hydrogen + ethylene)–air, and (helium + ethylene)–air diffusion flames at atmospheric pressure. The results indicate that although the addition of both hydrogen and helium to ethylene can reduce soot production, the addition of hydrogen is more effective. The addition of helium reduces soot formation only through dilution, while the addition of hydrogen suppresses soot formation through both dilution and direct chemical reaction. This conclusion is in agreement with the available experiments. The chemical effect of hydrogen addition is caused by the decrease of the hydrogen atom concentration in surface growth regions and the higher concentration of molecular hydrogen in the lower flame region.

## References

[1] J.R. Arthur, Nature 165 (1950) 557–558.

[2] P.A. Tesner, Proc. Combust. Inst. 7 (1958) 546–553.

[3] P.A. Tesner, H.J. Robinovitch, I.S. Rafalkes, Proc. Combust. Inst. 8 (1960) 801–806.

[4] P. Dearden, R. Long, J. Appl. Chem. 18 (1968) 243–251.

[5] D.X. Du, R.L. Axelbaum, C.K. Law, Combust. Flame 102 (1995) 11–20.

[6] Ö.L. Gülder, D.R. Snelling, R.A. Sawchuk, Proc. Combust. Inst. 26 (1996) 2351–2358.

[7] I. Glassman, Proc. Combust. Inst. 27 (1998) 1589–1596.

[8] K.K. Kuo, Principles of Combustion, Wiley, New York, 1986.

[9] M.W. Chase, C.A. Davies, J.R. Downey, D.J. Frurlp, R.A. McDonald, A.N. Syverud, JANAF Thermochemical Tables, third ed., Am. Chem. Soc. and Am. Inst. of Phys., New York, 1985.

[10] F. Liu, G.J. Smallwood, Ö.L. Gülder, J. Thermophys. Heat Transfer 14 (2000) 278–281.

[11] W.H. Dalzell, A.F. Sarofim, J. Heat Transfer 91 (1969) 100–104.

[12] R.J. Kee, G. Dixon-Lewis, J. Warnatz, M.E. Coltrin, J.A. Miller, Report No. SAND 86-8246, Sandia National Laboratories, 1986.

[13] H. Guo, F. Liu, G.J. Smallwood, Ö.L. Gülder, Int. J. Comput. Fluid Dyn. 18 (2004) 139–151.

[14] K.M. Leung, R.P. Lindstedt, W.P. Jones, Combust. Flame 871 (1991) 289–305.

[15] M. Fairwhether, W.P. Jones, X. Lindstedt, Combust. Flame 89 (1992) 45–63.

[16] H. Guo, F. Liu, G.J. Smallwood, Ö.L. Gülder, Proc. Combust. Inst. 29 (2002) 2359–2365.

[17] L. Talbot, R.K. Cheng, R.W.M. Schefer, D.R. Willis, J. Fluids Mech. 101 (1980) 737–758.

[18] J. Warnatz, U. Maas, R.W. Dibble, Combustion, third ed., Springer-Verlag, Berlin, 1999, p. 260.

[19] M. Frenklach, H. Wang, in: H. Bockhorn (Ed.), Soot Formation in Combustion: Mechanisms and Models, in: Springer Series in Chemical Physics, vol. 59, Springer-Verlag, Berlin, 1994, pp. 162–196.

[20] J. Appel, H. Bockhorn, M. Frenklach, Combust. Flame 121 (2000) 122–136.

[21] F. Xu, P.B. Sunderland, G.M. Faeth, Combust. Flame 108 (1997) 471–493.

[22] K.G. Neoh, J.B. Howard, A.F. Sarofim, in: D.C. Siegla, G.W. Smith (Eds.), Particulate Carbon: Formation During Combustion, Plenum, New York, 1981, pp. 261–282.

[23] S.V. Patankar, Numerical Heat Transfer and Fluid Flow, Hemisphere, New York, 1980.

[24] Z. Liu, C. Liao, C. Liu, S. McCormick, AIAA 95-0205, 1995.

[25] R.J. Kee, J.A. Miller, T.H. Jefferson, Sandia Report, SAND 80-8003, 1980.

[26] A. Kazakov, H. Wang, M. Frenklach, Combust. Flame 100 (1995) 111–120.